Supplemental Material for Constraints on heavy decaying dark matter from 570 days of LHAASO observations

LHAASO Collaboration,
S. Ando, M. Chianese, D. F.G. Fiorillo, G. Miele, and K. C.Y. Ng

The supplemental material is organized as follows. In Sec. I we describe in detail the regions of interest selected in the present analysis. In Sec. II, we describe the γ/hadron separation method. In Sec. III, we detail the method used to compute the detector response from Monte Carlo simulations. In Sec. IV we provide more details on the calculations of the DM signal and quantify the uncertainties related to the density profile choice, the background photons, and the galactic magnetic field. In Sec. V we report the constraints on the lifetime of DM particles for other decay channels. Finally, we compare with the latest IceCube results in Sec. VI.

I. REGIONS OF INTEREST

In Fig. S1 we show the selected regions of interest in the pixelated sky map with Galactic (left panel) and equatorial (right panel) coordinates. In Galactic coordinates (b, ℓ), they are centered at (30°,45°), (−35.2°,148.4°), (−35.1°,97.0°), (43.3°,183.3°), and (218.1°,77.0°). All the ROIs are 10 degrees away from the Galactic plane (dark band in the plots) and the Fermi bubbles, in order to reduce astrophysical contamination. The search region ROI_0 is expected to have the highest DM γ-ray flux due to its proximity to the Galactic center. $\mathrm{ROI}_1 - \mathrm{ROI}_4$ are control regions through which the isotropic cosmic-ray background is estimated, though their DM content is also taken into account. All the ROIs have the same angular size of 0.274 sr, and have the same declination as shown in the right plot. In Tab. S1, we report the energy-dependent D-factor, averaged over the ROIs, for the different energy bins. As the γ-ray energy increases, the D-factor decreases due to the γ-ray attenuation. Among the ROIs, the D-factor varies according to the NFW density profile.

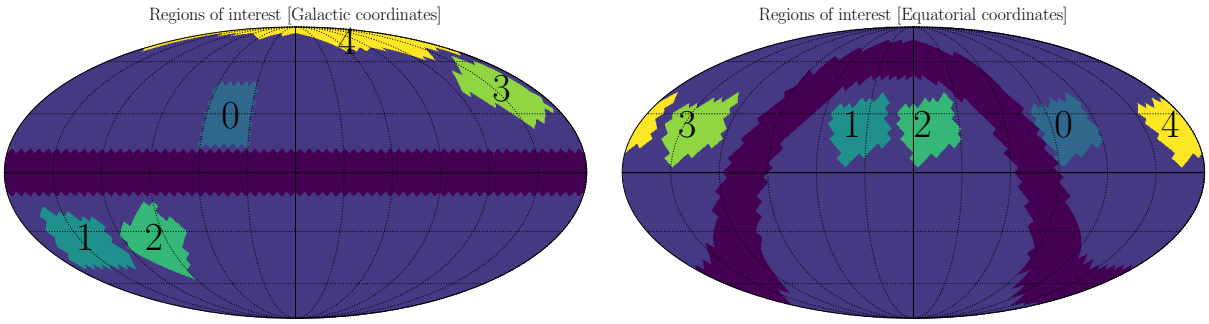

FIG. S1. Pixelated sky map highlighting the selected ROIs, labeled with indices from 0 to 4, in Galactic (left panel) and equatorial (right panel) coordinates. The dark band shows 10 degrees around the Galactic plane.

II. GAMMA/HADRON SEPARATION

The γ/hadron study of 1/2-KM2A has been detailed in the performance study [1]. We follow the same procedure in this work, but with a more stringent cut for the purpose of this study, as discussed below.

For each triggered event, we consider the discrimination parameter R,

$$R = \log \frac{N_\mu + 0.0001}{N_e}\,, \tag{S1}$$

where N_e is the number of electromagnetic particles measured by all the EDs with distance less than 200m from the shower core, and N_μ is the number of muons measured by all the MDs with distance less than 400m but further than 15m from the shower core. A cut at different R values corresponds to different γ-ray and cosmic-ray survival efficiencies. According to the proposed γ/hadron separation technique to identify primary cosmic rays and γ rays

$\log_{10}(E_\gamma/\mathrm{GeV})$	D-factor $[10^{22}\ \mathrm{GeV/cm^2}]$					$N_{\mathrm{DM}}(\mathrm{ROI}_0)$
	ROI_0	ROI_1	ROI_2	ROI_3	ROI_4	$\mathrm{DM} \to b\bar{b}$, $\tau_{\mathrm{DM}} = 6.3 \times 10^{28}\,\mathrm{s}$
5.0 – 5.2	2.68	1.18	1.55	1.20	1.60	83.6
5.2 – 5.4	2.59	1.13	1.49	1.15	1.54	41.9
5.4 – 5.6	2.22	0.96	1.26	0.97	1.31	20.8
5.6 – 5.8	1.66	0.73	0.95	0.74	0.98	6.6
5.8 – 6.0	1.24	0.57	0.73	0.58	0.76	1.7
6.0 – 6.2	1.02	0.49	0.62	0.50	0.64	0.4

TABLE S1. Dark matter D-factor for the NFW distribution averaged over the different ROIs for the 6 energy bins. The dependence on energy is completely due to the γ-ray absorption. The last column shows the expected number of detected events in the detector after γ/hadron separation for $b\bar{b}$ channel with $\tau_{\mathrm{DM}} = 6.3 \times 10^{28}$ s and $m_{\mathrm{DM}} = 10^7$ GeV. The τ_{DM} value is chosen to be that of the limit in Fig.1. Given the large DM mass, all energy bins receive contributions from DM decays. The values of N_{DM} is close to that of $2\sqrt{N_{\mathrm{ROI}_0}}$, showing that our limit is close to the statistical limit of the data, which highlights the importance of using the control regions as background estimates.

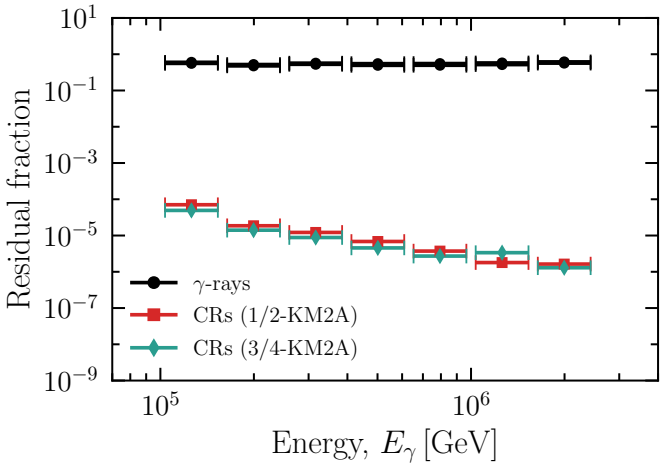

FIG. S2. The γ-ray and cosmic-ray survival fractions after γ/hadron separation. γ-ray events are obtained via simulation, while the cosmic-ray events are the actual 1/2-KM2A and 3/4-KM2A data.

by Ref. [2], we choose the selection criteria by maximizing the quality factor Q parameter to enhance the γ-ray observation significance in the case of background dominated sample [3].

$$Q = \frac{N_{\gamma,\mathrm{cut}}/N_\gamma}{\sqrt{N_{\mathrm{CR,cut}}/N_{\mathrm{CR}}}}\,, \tag{S2}$$

where N_γ ($N_{\gamma,\mathrm{cut}}$) and N_{CR} ($N_{\mathrm{CR,cut}}$) are the γ-ray and cosmic-ray events before (after) γ/hadron separation. The γ-ray survival fractions are obtained via Monte Carlo simulation, while we use the 1/2-KM2A data sets for cosmic-ray events. We also impose the condition that at least 50% of the γ-rays are kept after the cut. With this, the survival fractions of γ-ray (ϵ_γ) are slightly lower at 51.98%–61.51% from 125 TeV to 2 PeV compared to Ref. [1], but the cosmic-ray survival fractions (ϵ_{CR}) are further lowered by about one order of magnitude to 1.86×10^{-6} around 1 PeV, as shown in Fig. S2. To validate our new γ/hadron separation cut, we repeat the Crab Nebula analysis from Ref. [1], reproducing the Crab spectrum reported in Ref. [1] within statistical errors. This shows that our more stringent γ/hadron separation cut does not affect physical results. For γ/hadron separation with 3/4-KM2A data, we take the same cut as 1/2-KM2A, and the residual fraction is also shown in Fig. S2.

III. DETECTOR RESPONSE

To connect the detected number of events to physical quantities, the detector response to γ-rays is needed, which we obtain via Monte Carlo simulation. The primary γ-ray events in Monte Carlo simulation are produced from 10 TeV to 10 PeV and sampled uniformly in logarithm space with a power-law spectrum of spectral index -2. The sampling size $N_{\rm mc,orig}$ varies from 10^7 to 10^5 as energy increases. The simulated events are sampled according to the zenith angle (θ) dependence and geometrical efficiency ($\cos\theta$) of a flat detector, thus

$$N_{\rm mc,orig} \propto \sin\theta\cos\theta\,. \tag{S3}$$

The zenith angle is sampled from 0° to 70° with the azimuthal direction sampled completely.

The ROIs are each divided into 67 identical subpixels, each with sky area about $(3.7\,{\rm deg})^2$. Each subpixel is then tracked across the sky fully taking into account the detector runtime corrections and efficiencies. Consequently, the number of reference detector Monte Carlo events is given by

$$N_{\rm mc}(E_i,\theta_j) = \frac{N_{\rm mc,trig}(E_i,\theta_j)}{N_{\rm mc,orig}(E_i,\theta_j)} \int_{E_i} {\rm d}E \int {\rm d}\Omega\, \frac{{\rm d}I_{\rm mc}}{{\rm d}E}\, S\cos\theta_j T(\theta_j)\,, \tag{S4}$$

where ${\rm d}I_{\rm mc}/{\rm d}E \propto E^{-2}$ is the reference intensity spectrum, E_i is the energy bin considered, θ_j is the zenith angle from 0° to 50° in intervals of 1°, $N_{\rm mc,trig}(E_i,\theta_j)$ is the number of triggered events in the simulation [1], $N_{\rm mc,orig}(E_i,\theta_j)$ is the input number of events, S is the reference detector area, $T(\theta_j)$ is the time that the tracking point stays in the zenith angle considered over a day, and $\Omega_{\rm mc} = \int {\rm d}\Omega$ is the reference solid angle of the subpixel. The total number of reference Monte Carlo events ($N_{\rm mc}(E_i) = \sum_j N_{\rm mc}(E_i,\theta_j)$) is then summed over the zenith angles from 0° to 50°.

Using the reference events, for each subpixel, the physical intensity (${\rm d}I_{\rm data}/{\rm d}E$) corresponding to a number of detected events at each energy bin ($N_{\rm data}(E_i)$) is then given by

$$\frac{{\rm d}I_{\rm data}}{{\rm d}E} = \frac{N_{\rm data}}{N_{\rm mc}}\frac{\Omega_{\rm mc}}{\Omega_{\rm data}}\frac{T_{\rm mc}}{T_{\rm data}}\frac{{\rm d}I_{\rm mc}}{{\rm d}E}\,, \tag{S5}$$

where $T_{\rm mc} = \sum_j T(\theta_j)$, $T_{\rm data}$ is the actual observation time, and $\Omega_{\rm data}$ is the ROI solid angle. The physical intensity for each ROI is thus the averaged intensities of its subpixels.

IV. DETAILS ON THE DARK MATTER SIGNAL

Our limits are obtained by taking into account the prompt γ-ray component as well as the secondary Inverse-Compton (IC) component from Galactic DM decays. In Fig. S3, we show the DM γ-ray intensity from ${\rm ROI}_0$ obtained in case of different DM decay channels, for the benchmark case of DM particles with mass of 10 PeV and lifetime of 10^{28} s. The solid lines show the total flux given by the sum of the prompt (displayed with dashed lines) and secondary IC components. The additional contribution due to the secondary emission is highlighted by the shaded area. The fluxes stop at an energy of $m_{\rm DM}/2$, which is the maximum energy allowed in case of two-body DM decays. We emphasize that, even for neutrino channels, DM decays can produce primary γ-rays through high-order electroweak processes [4]. In the energy interval probed by LHAASO (from $10^{5.0}$ to $10^{6.2}$ GeV) the relative contribution of prompt and secondary components depends on the decay channel. As a rule of thumb, in case of DM particles decaying into quarks or electroweak bosons (left plot), the prompt component dominates over the secondary IC one for all the DM mass range considered. On the other hand, for leptophilic and neutrinophilic channels (middle and right plots, respectively) where primary electrons and positrons are produced at higher energies, the secondary IC component can dominate over the prompt one, especially in case of large DM masses. This can be seen in the figure by the size of the shaded areas.

The DM signals are affected by uncertainties that, in turn, impact our limits on the DM lifetime. In particular, both the prompt and the secondary components depend on the choice of the Galactic DM halo profile. In addition to the NFW profile, we also consider the Burkert (Bur) [5] and the Einasto (Ein) [6, 7] profiles:

$$\rho_h^{\rm Bur}(r) = \frac{\rho_s^{\rm Bur}}{\left(1+\frac{r}{r_s^{\rm Bur}}\right)\left(1+\left(\frac{r}{r_s^{\rm Bur}}\right)^2\right)} \qquad \text{and} \qquad \rho_h^{\rm Ein}(r) = \rho_s^{\rm Ein}\exp\left\{-\frac{2}{\alpha}\left[\left(\frac{r}{r_s^{\rm Ein}}\right)^{\alpha}-1\right]\right\} \tag{S6}$$

The scale radii are $r_s^{\rm Bur} = 9.26$ kpc and $r_s^{\rm Ein} = 20.0$ kpc, respectively, while the two normalizations $\rho_s^{\rm Bur}$ and $\rho_s^{\rm Ein}$ are fixed to yield a local DM density of 0.4 GeV cm^{-3}, in agreement with the case of NFW profile. For $b\bar{b}$ and $\tau^+\tau^-$ channels, we find that our limits change by less than 5% in case of the Burkert and Einasto profiles.

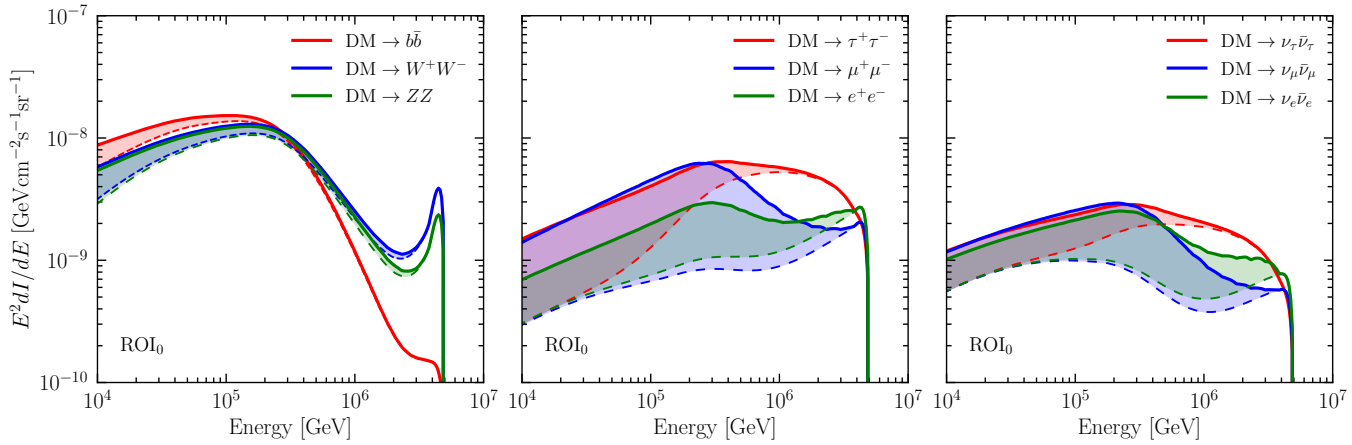

FIG. S3. Total DM γ-ray intensity (solid lines) from ROI$_0$ for the benchmark case of DM particles with 10^7 GeV mass and 10^{28} s lifetime. The dashed lines show the prompt Galactic component, while the shaded regions highlight the additional contribution due to the secondary Galactic IC component. Different colors correspond to different decay channels.

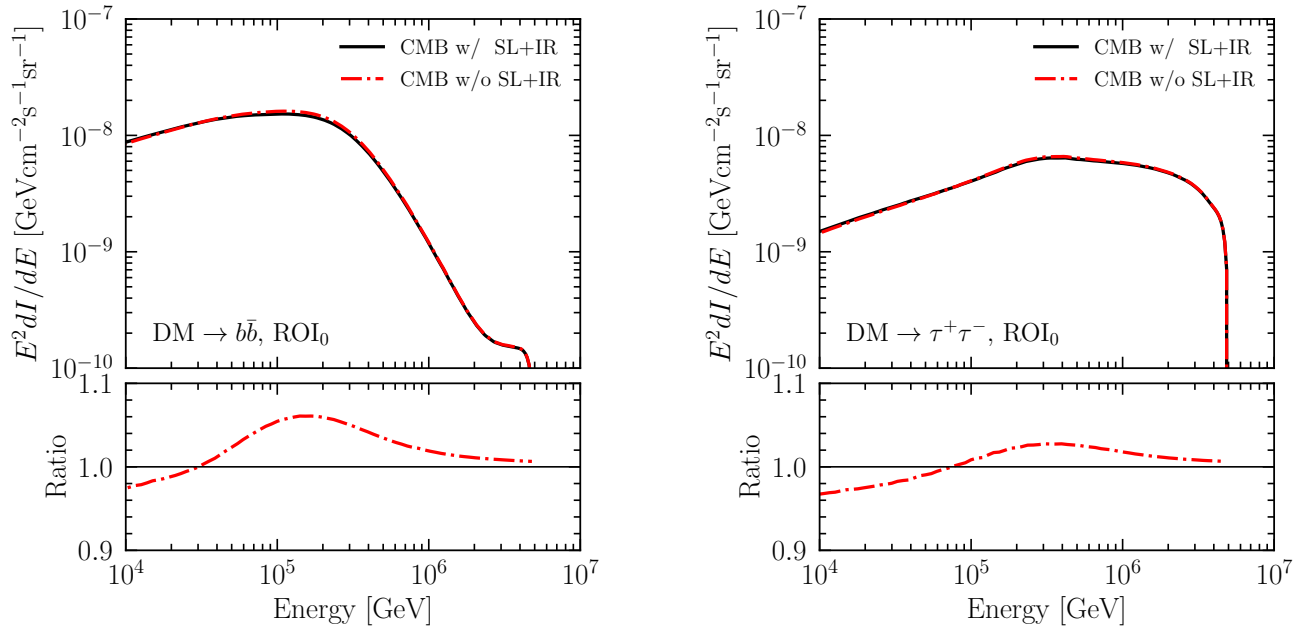

FIG. S4. Total γ-ray intensity from DM decays in ROI$_0$ obtained with (solid black lines) and without (dashed red lines) the SL+IR Galactic photon background, for $b\bar{b}$ and $\tau^+\tau-$ channels and with same parameters as Fig. S3. The lower panels show the ratio of the flux without SL+IR over the that with SL+IR.

An additional systematic uncertainty comes from the spectrum of background photons acting as targets for pair production and IC scatterings. Since the CMB is very well measured, such an uncertainty is completely related to the SL+IR background, which is typically sub-dominant with respect to the CMB. We estimate the uncertainties associated with SL+IR background by considering the DM flux with and without the SL+IR background, as shown in Fig. S4 for b quark and τ lepton channels for ROI$_0$. Ignoring SL+IR has two effects. One is that the flux between 10^5 GeV to 10^6 GeV are *enhanced* due to less γ-ray opacity in galaxy. The second is reduced flux due to less target photons for inverse-Compton scattering, but effect is mainly seen below 10^5 GeV, which is outside the range of our analysis. Overall these effects only change the flux by less than 10%. For the other ROIs, the effect of SL+IR background is even more sub-dominant due to the very small photon number density. Hence, the uncertainty on our limits related to the SL+IR photon background can be conservatively estimated to be smaller than 10%. We have also checked that the additional target photons from the extragalactic γ-ray background [8] is negligible compared to the SL+IR background in all the ROIs considered.

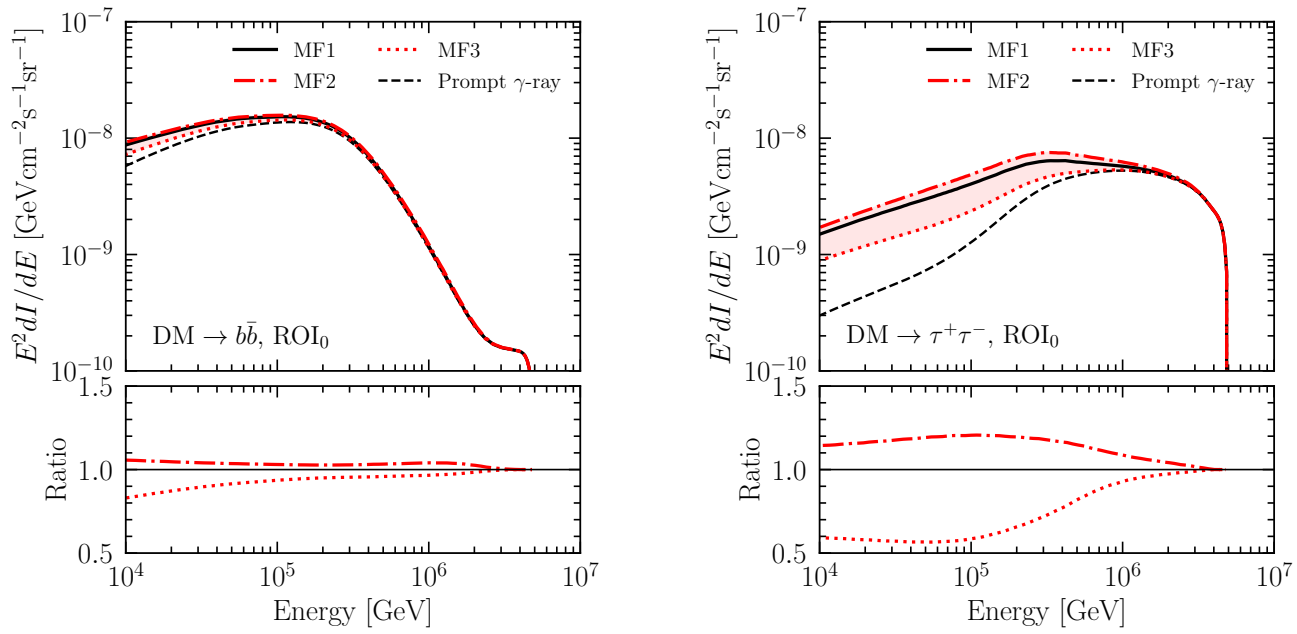

FIG. S5. Similar to Fig. S4, but for different MF models (see Eq.s (S7) and (S8)), as well as the unaltered prompt γ-ray component. The lower panels show the ratio of each case over the benchmark MF1 scenario (solid black line).

Finally, our calculations also depend on the Galactic Magnetic Field (MF) which determines the synchrotron energy losses of electrons and positrons injected by DM particles. As such, it only affect the secondary IC component which is sub-dominant in most of the DM scenarios analyzed. In particular, the higher the magnetic field, the more efficient are the synchrotron energy losses and consequently the secondary emission is more suppressed. To estimate the uncertainty due to the Galactic MF, we follow Ref. [9] and test three different configurations with the same position dependency:

$$B = B_0 \exp\left(-\frac{r - R_\odot}{r_D} - \frac{|z|}{z_D}\right) , \tag{S7}$$

where r and z are the radial distance and the height of the Galactic disk. The three MF models differ in the values assumed for the three parameters

$$\begin{aligned} &\text{MF1}: \ B_0 = 4.78\ \mu\text{G}, \ r_D = 10\ \text{kpc}, \ z_D = 2\ \text{kpc} \\ &\text{MF2}: \ B_0 = 5.1\ \mu\text{G}, \ r_D = 8.5\ \text{kpc}, \ z_D = 1\ \text{kpc} \\ &\text{MF3}: \ B_0 = 9.5\ \mu\text{G}, \ r_D = 30\ \text{kpc}, \ z_D = 4\ \text{kpc} \end{aligned} \tag{S8}$$

The model MF1 taken from Ref. [10] represents our benchmark scenario as discussed in the main text. In Fig. S5 we report the total γ-ray intensity obtained for different MF configurations, as well as the prompt γ-ray component (dashed black line). In the case of DM $\to b\bar{b}$ (left plot), the total flux is marginally affected (less than 10%) by the Galactic magnetic field as expected according to the sub-dominance of the secondary IC emission. On the other hand, for leptophilic and neutrinophilic channels, for which the case DM $\to \tau + \tau^-$ (right plot) is representative, the total flux can vary up to $\sim 50\%$. Nonetheless, in all the cases, the total flux including the secondary emission is always higher than the prompt component. Therefore, the limits obtained using the prompt component alone are conservative and robust.

V. ADDITIONAL DARK MATTER DECAY CHANNELS

In Fig. S6 we report the constraints on the DM lifetime obtained with the profile likelihood analysis for different DM decay channels. The limits displayed with solid lines are derived by including both prompt and secondary Galactic photons from decaying DM particles. The limits shown with dashed lines are obtained by taking into account only the prompt emission from DM decays and, therefore, are robust against the uncertainties described in the previous

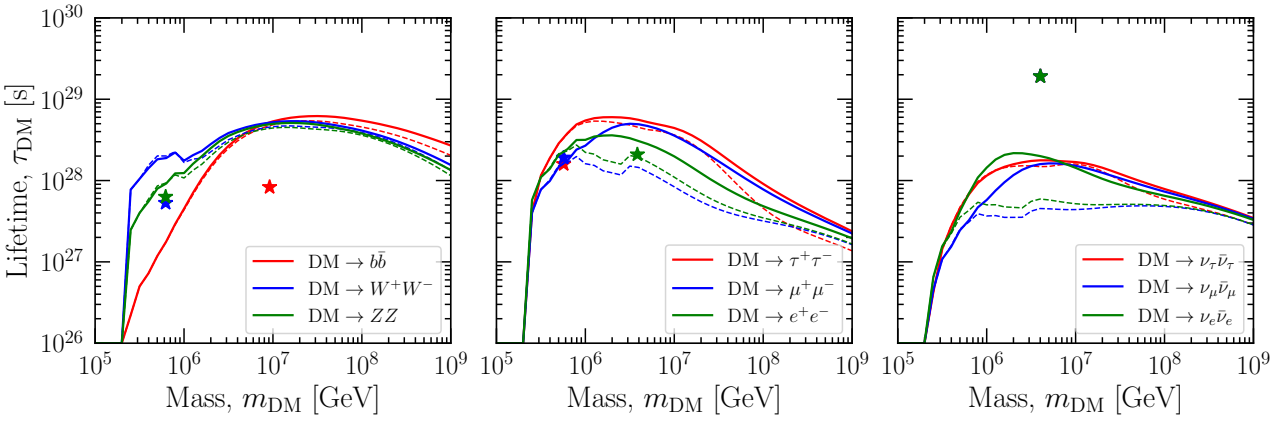

FIG. S6. Constraints at 95% CL on DM lifetime obtained with the profile likelihood analysis for the DM decay channels. The lines of the $b\bar{b}$ and $\tau^+\tau^-$ constraints corresponds to the ones reported in Fig. 1. The dashed lines correspond to the limits obtained considering only the prompt contribution from DM decay. The stars correspond to the best-fit scenario from the 7.5-year IceCube HESE data [11].

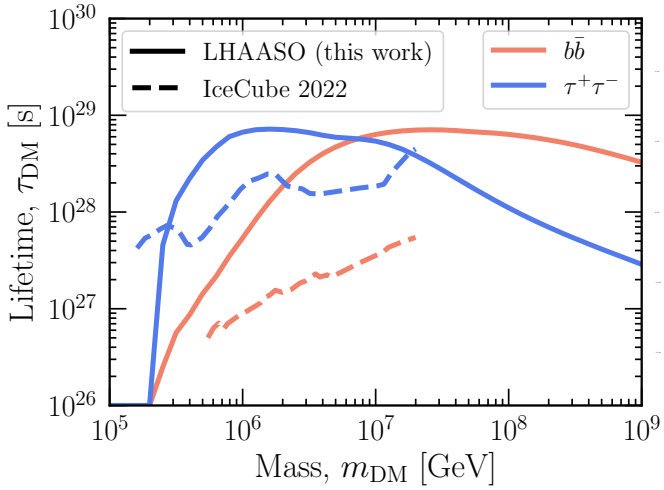

FIG. S7. Solid lines show the limits obtained in this work with LHAASO for $b\bar{b}$ (orange) and $\tau^+\tau^-$ (blue) channels, respectively. For comparison, in dashed lines, we show the limits from the most recent IceCube results [12].

section. In plots we also show the DM best-fit points (stars) obtained by analyzing the 7.5-year IceCube HESE data only under the DM interpretation of the diffuse high-energy neutrino flux [11]. The best-fit points differ from those reported in Fig. 1 (in the main text), which have also taken into account the 10-year IceCube through-going muon neutrino data (see Ref. [11] for more details). As can be seen from the figure, our results are in tension with the hypothesis of DM contributions in the diffuse high-energy neutrino flux for all the decay channels except for the neutrinophilic ones (right panel).

VI. COMPARISON WITH ICECUBE

Figure. S7 shows the comparison of our limits with the latest IceCube results from Ref. [12]. In the two channels considered ($b\bar{b}$ and $\tau^+\tau^-$), our results are generally stronger. However, IceCube would be stronger in channels involving neutrino finals states, which highlights the complementarity between γ-ray and neutrino detectors.

[1] F. Aharonian *et al.*, "The observation of the Crab Nebula with LHAASO-KM2A for the performance study," Chin. Phys. C **45**, 025002 (2021), arXiv:2010.06205 [astro-ph.HE].

[2] V.V Bugayov, A.V Plyasheshnikov, V.V Vassiliev, and T.C Weekes, "On the application of differences in intrinsic fluctuations of cherenkov light images for separation of showers," Astroparticle Physics **17**, 41–50 (2002).

[3] T. P. Li and Y. Q. Ma, "Analysis methods for results in gamma-ray astronomy." ApJ **272**, 317–324 (1983).

[4] Christian W. Bauer, Nicholas L. Rodd, and Bryan R. Webber, "Dark matter spectra from the electroweak to the Planck scale," JHEP **06**, 121 (2021), arXiv:2007.15001 [hep-ph].

[5] A. Burkert, "The Structure of dark matter halos in dwarf galaxies," Astrophys. J. Lett. **447**, L25 (1995), arXiv:astro-ph/9504041.

[6] Julio F. Navarro, Eric Hayashi, Chris Power, Adrian Jenkins, Carlos S. Frenk, Simon D. M. White, Volker Springel, Joachim Stadel, and Thomas R. Quinn, "The Inner structure of Lambda-CDM halos 3: Universality and asymptotic slopes," Mon. Not. Roy. Astron. Soc. **349**, 1039 (2004), arXiv:astro-ph/0311231.

[7] Alister W. Graham, David Merritt, Ben Moore, Juerg Diemand, and Balsa Terzic, "Empirical models for Dark Matter Halos. I. Nonparametric Construction of Density Profiles and Comparison with Parametric Models," Astron. J. **132**, 2685–2700 (2006), arXiv:astro-ph/0509417.

[8] Alberto Franceschini and Giulia Rodighiero, "The extragalactic background light revisited and the cosmic photon-photon opacity," Astron. Astrophys. **603**, A34 (2017), arXiv:1705.10256 [astro-ph.HE].

[9] Jatan Buch, Marco Cirelli, Gaëlle Giesen, and Marco Taoso, "PPPC 4 DM secondary: A Poor Particle Physicist Cookbook for secondary radiation from Dark Matter," JCAP **09**, 037 (2015), arXiv:1505.01049 [hep-ph].

[10] Andrew W. Strong, Igor V. Moskalenko, and Olaf Reimer, "Diffuse continuum gamma-rays from the galaxy," Astrophys. J. **537**, 763–784 (2000), [Erratum: Astrophys.J. 541, 1109 (2000)], arXiv:astro-ph/9811296.

[11] Marco Chianese, Damiano F. G. Fiorillo, Gennaro Miele, Stefano Morisi, and Ofelia Pisanti, "Decaying dark matter at IceCube and its signature on High Energy gamma experiments," JCAP **11**, 046 (2019), arXiv:1907.11222 [hep-ph].

[12] R. Abbasi *et al.* (IceCube), "Searches for Connections between Dark Matter and High-Energy Neutrinos with IceCube," (2022), arXiv:2205.12950 [hep-ex].